HHS Public Access

Author manuscript

*Magn Reson Med*. Author manuscript; available in PMC 2023 March 01.

Published in final edited form as:

*Magn Reson Med*. 2022 March ; 87(3): 1490–1499. doi:10.1002/mrm.29040.

# Utilizing Flip Angle/TR Equivalence to Reduce Breath hold Duration in Hyperpolarized $^{129}$Xe 1-Point Dixon Gas Exchange Imaging

**Peter J. Niedbalski**[1,*], **Junlan Lu**[2], **Chase S. Hall**[1], **Mario Castro**[1], **John P. Mugler III**[3], **Yun M. Shim**[4], **Bastiaan Driehuys**[5]

[1]Division of Pulmonary, Critical Care, and Sleep Medicine, University of Kansas Medical Center, Kansas City, Kansas, USA

[2]Medical Physics Graduate Program, Duke University, Durham, North Carolina, USA

[3]Center for In-vivo Hyperpolarized Gas MR Imaging, Department of Radiology and Medical Imaging, University of Virginia, Charlottesville, Virginia, USA

[4]Department of Medicine, Division of Pulmonary and Critical Care Medicine, University of Virginia School of Medicine, Charlottesville, Virginia, USA.

[5]Department of Radiology, Duke University Medical Center, Durham, North Carolina, USA

## Abstract

**Purpose:** To reduce scan duration in hyperpolarized $^{129}$Xe 1-point Dixon gas exchange imaging by utilizing flip angle (FA)/TR equivalence.

**Methods:** Images were acquired in 12 subjects (N = 3 radiation therapy, N = 1 unexplained dyspnea, N = 8 Healthy) using both standard (TR = 15 ms, FA = 20°, Duration = 15 s, 998 projections) and “fast” (TR = 5.4 ms, FA = 12°, Duration = 11.3 s, 2100 projections) acquisition parameters. For the “fast” acquisition, three image sets were reconstructed using subsets of 1900, 1500, and 1000 projections. From the resulting ventilation, tissue (“barrier”), and red blood cell (RBC) images, image metrics and biomarkers were compared to assess agreement between methods.

**Results:** Images acquired using both FA/TR settings had similar qualitative appearance. There were no significant differences in SNR, image mean, or image standard deviation between images. Moreover, the percentage of the lungs in “defect”, “normal”, and “high” bins for each image (ventilation, RBC, Barrier) was not significantly different among the acquisition types. After registration, comparison of 3D image metrics (Dice, volume similarity, average distance) agreed well between bins. Images using 1000 projections for reconstruction had no significant differences from images using all projections.

**Conclusion:** Using flip angle/TR equivalence, hyperpolarized $^{129}$Xe gas exchange images can be acquired via the 1-point Dixon technique in as little as 6 s, compared to ~15 s for previously

[*]Corresponding Author: Peter J. Niedbalski, 3901 Rainbow Blvd. Lied 3043, Kansas City, KS 66160, 913-588-2271, pniedbalski@kumc.edu.

reported parameter settings. The resulting images from this accelerated scan have no significant differences from the standard method in qualitative appearance or quantitative metrics.

**Keywords**

Hyperpolarized $^{129}$Xe; Gas Exchange; 1-Point Dixon; Flip Angle/TR equivalence

## Introduction

Hyperpolarized (HP) $^{129}$Xe MRI uniquely enables the regional quantification of pulmonary gas exchange by imaging xenon gas dissolved in red blood cells (RBCs) and other pulmonary tissues (“barrier”) (1). Within these compartments, $^{129}$Xe has distinct chemical shift values (gas: 0 ppm, barrier: 197 ppm, RBC: 218 ppm) which enables spectroscopy (2–7) and imaging of pulmonary gas exchange (1,8–11) using both single-point (8,12,13) and multi-point methods (9–11,14,15). To date, the most widely studied is the 1-Point Dixon method, which uses an interleaved, 3D radial acquisition on the gas and dissolved frequencies to simultaneously image both gaseous and dissolved xenon within the same ~15 s breath-hold (8). The RBC and barrier components are separated by beginning the radial readout at an echo time (TE90) at which these signal components are 90° out of phase.

All published implementations of gas exchange HP $^{129}$Xe MRI utilize comparatively high radio frequency (RF) pulse flip angle (FA) (≥20°) for dissolved-phase excitation and repetition time (TR) sufficiently long to allow time for exchange to occur between gaseous and dissolved compartments (often 15 ms between dissolved excitations, which determines dissolved image contrast) (8–14,16–20). This allows for reasonable signal-to-noise ratio (SNR) in dissolved phase images (SNR = 10–25 for Barrier, 5–10 for RBC) but limits the number of views that can be acquired. With the requirement of sampling within a breath-hold (≲16 s), TR = 15 ms limits the maximum total number of views to 1067 (often 1000 for a 15 s breath-hold), thereby requiring coarse resolution or heavy undersampling. Moreover, such long breath-hold durations may be challenging for subjects with severe lung disease.

Notably the 1-point Dixon sequence reported in the literature uses only ~5–6 ms of its 15ms TR for signal acquisition (8), (Figure 1). However, reducing TR reduces the available exchange time between gaseous and dissolved compartments, impacting both SNR and quantitative imaging biomarkers. To this end, Ruppert et al. proposed a theoretical framework by which TR may be shortened without sacrificing SNR or information content of images (21). Specifically, FA and TR for a given dissolved HP $^{129}$Xe measurement can be converted to a standardized metric termed $TR_{90°,equiv}$. Using this “FA/TR equivalence”, TR of a dissolved phase acquisition can be changed in concert with the FA to maintain the same $TR_{90°,equiv}$. Here we use this FA/TR equivalence to reduce TR and shorten scan time for gas exchange imaging using hyperpolarized $^{129}$Xe 1-Point Dixon imaging.

# Methods

## Subjects

All human studies were approved by the Duke University IRB and the FDA. A total of 12 subjects were imaged, including N = 3 “young” healthy subjects (2 female, age 25.7 ± 2.3), N = 5 “old” healthy subjects (4 female, age 69.4 ± 10.2), N = 3 radiation therapy patients (3 male, age 75.7 ± 13.7), and N = 1 patient with unexplained dyspnea (Female, age 39).

## Xenon Polarization and Delivery

Enriched xenon gas (>80% $^{129}$Xe, Linde Specialty Gases, Stewartsville, NJ) was polarized to ~50% using a Polarean 9820 hyperpolarizer (Polarean Imaging, Plc, Durham, NC). The total dose volume used was equal to 20% of subject forced vital capacity (FVC), with between 60 and 100% of the total dose composed of hyperpolarized $^{129}$Xe. The balance of the dose was a mixture of 90% helium and 9% nitrogen. While this strategy of changing the percentage of xenon in the dose can affect the mean molecular weight of the gas, it minimizes the adverse event protocol, optimizes signal to noise, and should have little impact on gas exchange metrics.

## Hyperpolarized $^{129}$Xe Imaging

As described by Ruppert (21), for a given combination of TR and FA, $\alpha$,

$$TR_{90^\circ, equiv} = \frac{TR}{1 - \cos(\alpha)}$$

Thus, for the commonly reported 1-Point Dixon imaging parameters (TR = 15 ms, FA = 20°), $TR_{90°,equiv}$=249 ms. This same $TR_{90°,equiv}$ can be obtained for a hardware- and sequence-limited TR of 5.4 ms, using FA = 12°. The expected RBC and Barrier signal intensity can be modeled for both FA/TR combinations by using the model of xenon exchange (MOXE) (6). Briefly, signal recovery was modeled for both FA/TR combinations using literature values for septal wall thickness (22), barrier thickness (23), capillary transit time,(24) tissue diffusion coefficient (25), and xenon solubility (26). As illustrated in Figure 1, RBC and Barrier signal are expected to be equivalent for these two sets of imaging parameters, implying that both can be analyzed using the same reference distributions.

Subjects were positioned supine in a 3T MRI scanner (Siemens TRIO, Siemens, Erlangen, Germany) with a flexible $^{129}$Xe vest coil (Clinical MR Solutions, Brookfield, WI) over their chest. A calibration spectroscopy sequence (13), was performed to fine-tune the resonant frequency of gaseous and dissolved xenon and transmitter settings, while determining the global RBC/Barrier ratio and TE90 (TE at which RBC and Barrier signals are 90° out of phase). Parameters for this calibration sequence include RF excitation using a 0.69ms, 1-lobe windowed sinc, TR/TE = 15/0.45 ms, FA = 20°, Bandwidth = 25.6 kHz, Number of Samples = 256, Number of FIDs =500 and 20 at the dissolved and gaseous xenon frequencies, respectively,. This single acquisition was used to calibrate imaging parameters for both standard and fast acquisitions, as justified in Supporting Information Section S1, Figures S1 and S2.

Following calibration, subjects were imaged using “standard” and “fast” 1-point Dixon acquisitions. Parameters identical for both acquisitions included: matrix size = 64 × 64 × 64, field of view = 400 × 400 × 400 $mm^3$, dwell time = 10 μs, bandwidth = 781 Hz/pixel, readout duration = 0.64 ms, gas FA = 0.5°, RF excitation using a 0.69ms 1-lobe, windowed sinc,,projection ordering = Halton-randomized spiral (13). Parameters specific to the “standard” acquisition included: TR = 15ms, dissolved FA = 20°, number of radial projections = 998 (on each gas and dissolved), scan duration = 15 s. Parameters specific to the “fast” acquisition included: TR = 5.4 ms, Dissolved FA = 12°, number of radial projections = 2100, scan duration = 11.3 s. The mean ± standard deviation xenon dose equivalent (27) for standard acquisitions was 152 ± 37 mL, and for fast acquisitions was 159 ± 36 mL.

Following gas exchange imaging, a thoracic cavity image was acquired without moving the subject, using the body coil with a geometry-matched $^1H$ 3D radial acquisition during a volume-matched breath-hold of room air. Parameters include: 0.5ms hard pulse excitation, TR/TE = 2.3/0.4 ms, bandwidth = 781 Hz/Pixel, number of radial projections = 4600, scan duration = 12 s This image was used to generate a thoracic cavity mask for image analysis.

## Image Reconstruction and Analysis

Images were reconstructed and analyzed using MATLAB 2020a (Mathworks, Natick, MA). Reconstruction included iterative density compensation and regridding (28,29) implemented in an open source Matlab package (30). To avoid contamination from downstream magnetization arising from the larger vasculature, the first 60(200) projections were discarded for the standard(fast) image acquisitions. Using TR = 5.4 ms enabled acquiring more projections than the traditional implementation, and thus images could be reconstructed from smaller subsets to investigate different levels of undersampling. This included: Standard using all (938) projections (“Standard”), Fast using all (1900) projections (“Fast”), Fast using 1500 projections (“Fast1500”), and Fast using 1000 projections (“Fast1000”). All were reconstructed using identical parameters (i.e. density compensation, kernel size, overgridding).

Anatomic images were reconstructed and the lungs automatically segmented using a convolutional neural network (CNN) deep learning algorithm implemented in Python 3.7 (31,32).

1-Point Dixon Images were analyzed as described by Wang et al (20). Briefly, dissolved phase images were separated into their constituent RBC and Barrier images by performing a phase shift such that the mean RBC/Barrier ratio within the lung mask matched the global spectroscopic RBC/Barrier. The resulting ventilation, barrier/gas, and RBC/gas images were binned (Ventilation and RBC: 6 bins, barrier: 8 bins) using means and standard deviations from a healthy reference population of young (age 20–35), healthy individuals.

All statistical analysis was performed in IBM SPSS Statistics Version 26.0 (IBM, Armonk, NY). Whole lung values for SNR, image means, and image standard deviations were compared among the four reconstructed datasets using Bland Altman analysis and repeated measures analysis of variance (ANOVA). For Bland Altman analysis, Fast, Fast1500, and

Fast1000 reconstructions were compared to the Standard reconstruction. In addition to whole-lung measurements, the percentage of the lungs in each analysis bin was compared using Bland Altman Analysis and repeated measures ANOVA with post-hoc pairwise T-tests.

To assess regional agreement between different image sets acquired in separate breath-holds, barrier and RBC images from Fast, Fast1500, and Fast1000 reconstructions were registered to those from Standard reconstruction using ANTSpy (33). Briefly, after registering the "Fast" ventilation images to the "Standard" ones, the same transformation was applied to RBC and Barrier images. Then, images were binned, as described above, confined within the mask of the standard image. To simplify analysis, the two lowest bins were combined to a single "bin 1", the two highest combined to a single "bin 3", and all other bins combined into a single "bin 2". These registered, binned maps were compared using Dice coefficients and average difference metrics (34). Additionally, bin volumes from pre-registered images were compared using the volume similarity metric (34). For Dice coefficients and volume similarity, a value of 1 indicates perfect agreement; for the average distance metric, a value of 0 indicates perfect agreement.

## Results

For all subjects and acquisitions, all four cases were successfully reconstructed. Qualitatively, images had similar appearance and quality (Figure 2A, 2B), and line profiles over the images show that all images have similar resolution (Figure 2C–2H).

The gas images of healthy subjects had mean SNR ranging from 15 for Standard to 21 for Fast1000 (Table 1). Total dissolved image SNR was lowest for Fast with a mean of 15, and highest for Fast1000 and Standard with a mean of 23. Once dissolved images were separated into their constituent RBC and barrier images, Fast1000 and Standard had the highest SNR in both barrier (mean 15) and RBC (mean 8), while the Fast reconstruction had the lowest SNR for both barrier (mean 9) and RBC (mean 5).

The mean signal within the masked volume was not significantly different among the four image sets for ventilation ($p = 0.62$), barrier/gas ($p = 0.33$), or RBC/gas ($p = 0.29$) (Table 1). Furthermore, it exhibited no systematic deviation between the fast acquisition (for any of the three reconstructions) and the standard acquisition as shown by Bland Altman analysis (Figure 3). Moreover, the "spread" of data was similar for all four image sets, with no significant differences among the standard deviation within the masked volume for ventilation ($p = 0.29$), barrier ($p = 0.19$), or RBC ($p = 0.39$). Bland Altman analysis on the standard deviation of the masked volume similarly showed minimal systematic difference between fast acquisitions and standard acquisitions (Supporting Information Figure S3).

Binned maps showed good visual agreement between standard and fast acquisitions (Figure 4). The percentage of lung voxels in each bin was not significantly different among the 4 different image sets for any of the 6 ventilation, 8 Barrier, or 6 RBC bins ($p > 0.08$ for all cases). Bland Altman analysis showed minimal systematic difference in the volume in each bin between the fast and standard acquisitions (Supporting Information Figures S4–S6).

Regional comparison of images showed the best agreement for bin 2 of both barrier and RBC, with Dice coefficients and volume similarity near 1 and average distance near 0 (Figure 4). Bin 1 showed moderate agreement for all three metrics in both RBC and Barrier, while Bin 3 showed relatively poor agreement for all metrics. Overall agreement as measured by the weighted average of Dice coefficients was strong (Figure 4C). Agreement between fast and standard acquisitions was not significantly different between the three reconstructions for any of the bin or metric comparisons.

## Discussion

Compared with using standard, 15-ms TR for 1-point Dixon-based gas exchange imaging, the fast approach has several advantages. Gas images have considerably higher SNR without sacrificing spatial resolution. This is expected due to faster sampling, which mitigates $T_1$ relaxation, and a two-fold increase in sampling percentage (35). Moreover, the use of a smaller FA for dissolved phase excitation reduces gas depolarization via exchange with depleted dissolved magnetization, which could partially explain the high SNR in sub-sampled images (36). For dissolved-phase images, those reconstructed with all projections have slightly reduced SNR and equivalent resolution. This reduction in SNR when using 1900 projections for reconstruction is likely due to lower gas signal in the final projections of the scan due to magnetization depletion from the previous RF pulses. However, in all cases, SNR is adequate for analysis, minimizing this concern.

More importantly, quantitative metrics from the four reconstructed image sets were similar. Specifically, ventilation, barrier/gas, and RBC/gas had similar range of values, means, and standard deviations (Table 1). This was true for both healthy subjects and radiation therapy subjects (37), indicating similarity between acquisitions, even for imaging impaired lung function. Moreover, using binning analysis (20) on images acquired with short TR yielded maps that were visually similar to those acquired with the standard acquisition. For combined bins 1 and 2 (i.e. low and normal), volume similarity and regional overlap between fast and standard acquisitions was good to moderate. For bin 3 (high) the agreement was poorer, particularly for Barrier images. This is due to the population imaged in this study (mostly healthy), who have relatively small and few regions of high barrier and high RBC, thereby confounding the use of 3D image comparison metrics. Some of the differences in binned maps could also be due to reduced gas-phase depolarization via exchange in the case of the fast acquisition. While gas depolarization is controlled for by scaling barrier and RBC images by the gas image, significant intra-voxel heterogeneity could affect these ratios. Thus, the reduced depolarization in the fast acquisition may lead to more physically accurate dissolved xenon metrics. Finally, the same healthy cohort binning thresholds were used for both standard and fast images, which could impact the agreement between binned maps, though FA/TR equivalence suggests that this impact should be minimal.

This study has several limitations. Due to logistical constraints, one calibration scan using standard parameters (FA = 20°, TR = 15 ms) was used to calibrate TE90 and RBC/Barrier for both scans. This is justified by the FA/TR equivalence principle, but there may be subtle differences that could impact quantitative markers. Additionally, the initial projections

of image acquisitions contained downstream magnetization, which required discarding 60 (200) projections for standard (fast) acquisitions. This can be easily mitigated by applying dummy RF pulses to the dissolved magnetization to reach steady state more quickly. Moreover, we only imaged 3 subjects with known lung disease. While imaging subjects with known pathophysiology would provide further evidence of the similarity of the standard and fast methods, the subjects imaged in the present work make a compelling case that FA/TR equivalence can be effectively used to shorten HP $^{129}$Xe gas exchange imaging. We also note that the current study only explored one FA/TR combination that intentionally maintained the same $TR_{90,equiv}$ as the parameters most commonly reported in the literature. It may be that utilizing a longer $TR_{90,equiv}$ could provide higher RBC signal, provided that $TR_{90,equiv}$ remains short enough to avoid downstream magnetization.

Finally, we note that multiple-echo methods of gas exchange imaging similarly have periods of dead time within the pulse sequence (9–11). The present findings should be generalizable to these methods, enabling increased sampling percentage, shortened breath-holds, higher resolution, or some combination of these.

## Conclusion

Hyperpolarized $^{129}$Xe gas exchange imaging using the 1-point Dixon method has demonstrated impressive sensitivity to disease state, but its implementation in those with severe lung disease is challenging due to the requirement of a long (~15s) breath-hold. Using flip-angle/TR equivalence for dissolved phase hyperpolarized $^{129}$Xe MRI, we have demonstrated that TR (and thus scan duration) can be significantly reduced with no loss of qualitative image quality or quantitative imaging biomarkers. By shortening TR, we were able to improve the sampling percentage of images 2-fold over standard imaging parameters while reducing breath-hold duration to ~11s. Images acquired using this accelerated method exhibited no significant differences from the standard images in dissolved-phase signal intensity, image mean, image standard deviation, or bin volumes. Moreover, reconstructions using subsets of radial projections demonstrated that 1-point Dixon images using 1000 projections with shortened TR and small flip angle provide comparable images to the standard acquisition, potentially enabling gas exchange imaging in only a 6s breath-hold. Ultimately, these results demonstrate that, by employing flip-angle/TR equivalence, HP $^{129}$Xe gas exchange MRI can be reduced in duration, making this method more clinically feasible.

## Supplementary Material

Refer to Web version on PubMed Central for supplementary material.

## Acknowledgements

This work was supported by the NIH (UL1TR002366, 3UL1TR003015, NHLBI: R01HL132177, R01HL105643 and R01HL126771), the NSF Graduate Research Fellowships Program (DGE-1644868), and Polarean Imaging Plc. The authors thank Zackary I. Cleveland and Matthew M. Willmering for helpful discussions.

## References


1. Driehuys B, Cofer GP, Pollaro J, Mackel JB, Hedlund LW, Johnson GA. Imaging alveolar-capillary gas transfer using hyperpolarized Xe-129 MRI. Proc Natl Acad Sci USA 2006;103(48):18278–18283. [PubMed: 17101964]
2. Collier GJ, Marshall H, Rao M, Stewart NJ, Capener D, Wild JM. Observation of cardiogenic flow oscillations in healthy subjects with hyperpolarized 3He MRI. J Appl Physiol 2015;119(9):1007–1014. [PubMed: 26338461]
3. Norquay G, Leung G, Stewart NJ, Tozer GM, Wolber J, Wild JM. Relaxation and exchange dynamics of hyperpolarized 129Xe in human blood. Magn Reson Med 2015;74(2):303–311. [PubMed: 25168398]
4. Norquay G, Leung G, Stewart NJ, Wolber J, Wild JM. 129Xe chemical shift in human blood and pulmonary blood oxygenation measurement in humans using hyperpolarized 129Xe NMR. Magn Reson Med 2017;77(4):1399–1408. [PubMed: 27062652]
5. Weatherley ND, Stewart NJ, Chan H-F, Austin M, Smith LJ, Collier G, Rao M, Marshall H, Norquay G, Renshaw SA, Bianchi SM, Wild JM. Hyperpolarised xenon magnetic resonance spectroscopy for the longitudinal assessment of changes in gas diffusion in IPF. Thorax 2019;74(5):500–502. [PubMed: 30389827]
6. Chang YLV. MOXE: A model of gas exchange for hyperpolarized 129Xe magnetic resonance of the lung. Magn Reson Med 2013;69(3):884–890. [PubMed: 22565296]
7. Ruppert K, Altes TA, Mata JF, Ruset IC, Hersman FW, Mugler III JP. Detecting pulmonary capillary blood pulsations using hyperpolarized xenon-129 chemical shift saturation recovery (CSSR) MR spectroscopy. Magn Reson Med 2016;75(4):1771–1780. [PubMed: 26017009]
8. Kaushik SS, Robertson SH, Freeman MS, He M, Kelly KT, Roos JE, Rackley CR, Foster WM, McAdams HP, Driehuys B. Single-Breath Clinical Imaging of Hyperpolarized Xe-129 in the Airspaces, Barrier, and Red Blood Cells Using an Interleaved 3D Radial 1-Point Dixon Acquisition. Magn Reson Med 2016;75(4):1434–1443. [PubMed: 25980630]
9. Qing K, Ruppert K, Jiang Y, Mata JF, Miller GW, Shim YM, Wang C, Ruset IC, Hersman FW, Altes TA, Mugler JP. Regional Mapping of Gas Uptake by Blood and Tissue in the Human Lung Using Hyperpolarized Xenon-129 MRI. J Magn Reson Imaging 2014;39(2):346–359. [PubMed: 23681559]
10. Kammerman J, Hahn AD, Cadman RV, Malkus A, Mummy D, Fain SB. Transverse relaxation rates of pulmonary dissolved-phase Hyperpolarized 129Xe as a biomarker of lung injury in idiopathic pulmonary fibrosis. Magn Reson Med 2020;84(4):1857–1867. [PubMed: 32162357]
11. Collier GJ, Eaden JA, Hughes PJC, Bianchi SM, Stewart NJ, Weatherley ND, Norquay G, Schulte RF, Wild JM. Dissolved 129Xe lung MRI with four-echo 3D radial spectroscopic imaging: Quantification of regional gas transfer in idiopathic pulmonary fibrosis. Magn Reson Med 2021;85(5):2622–2633. [PubMed: 33252157]
12. Hahn AD, Kammerman J, Evans M, Zha W, Cadman RV, Meyer K, Sandbo N, Fain SB. Repeatability of regional pulmonary functional metrics of Hyperpolarized 129Xe dissolved-phase MRI. J Magn Reson Imaging 2019;50(4):1182–1190. [PubMed: 30968993]
13. Wang Z, He M, Bier E, Rankine L, Schrank G, Rajagopal S, Huang YC, Kelsey C, Womack S, Mammarappallil J, Driehuys B. Hyperpolarized 129Xe gas transfer MRI: the transition from 1.5T to 3T. Magn Reson Med 2018;80(6):2374–2383. [PubMed: 30024058]
14. Doganay O, Chen M, Matin T, Rigolli M, Phillips J-A, McIntyre A, Gleeson FV. Magnetic resonance imaging of the time course of hyperpolarized (129)Xe gas exchange in the human lungs and heart. Eur Radiol 2019;29(5):2283–2292. [PubMed: 30519929]
15. Doganay O, Wade T, Hegarty E, McKenzie C, Schulte RF, Santyr GE. Hyperpolarized 129Xe imaging of the rat lung using spiral IDEAL. Magn Reson Med 2016;76(2):566–576. [PubMed: 26332385]
16. Hahn AD, Kammerman J, Fain SB. Removal of hyperpolarized 129Xe gas-phase contamination in spectroscopic imaging of the lungs. Magn Reson Med 2018;80(6):2586–2597. [PubMed: 29893992]

17. Rankine LJ, Wang Z, Wang JM, He M, McAdams HP, Mammarappallil J, Rackley CR, Driehuys B, Tighe RM. 129Xenon Gas Exchange Magnetic Resonance Imaging as a Potential Prognostic Marker for Progression of Idiopathic Pulmonary Fibrosis. Ann Am Thorac Soc 2020;17(1):121–125. [PubMed: 31593488]
18. Wang JM, Robertson SH, Wang Z, He M, Virgincar RS, Schrank GM, Smigla RM, O'Riordan TG, Sundy J, Ebner L, Rackley CR, McAdams P, Driehuys B. Using hyperpolarized (129)Xe MRI to quantify regional gas transfer in idiopathic pulmonary fibrosis. Thorax 2018;73(1):21–28. [PubMed: 28860333]
19. Wang Z, Bier EA, Swaminathan A, Parikh K, Nouls J, He M, Mammarappallil JG, Luo S, Driehuys B, Rajagopal S. Diverse Cardiopulmonary Diseases are Associated with Distinct Xenon MRI Signatures. Eur Respir J 2019;54(6):1900831. [PubMed: 31619473]
20. Wang Z, Robertson SH, Wang J, He M, Virgincar RS, Schrank GM, Bier EA, Rajagopal S, Huang YC, O'Riordan TG, Rackley CR, McAdams HP, Driehuys B. Quantitative analysis of hyperpolarized 129Xe gas transfer MRI. Med Phys 2017;44(6):2415–2428. [PubMed: 28382694]
21. Ruppert K, Amzajerdian F, Hamedani H, Xin Y, Loza L, Achekzai T, Duncan IF, Profka H, Siddiqui S, Pourfathi M, Sertic F, Cereda MF, Kadlecek S, Rizi RR. Assessment of flip angle–TR equivalence for standardized dissolved-phase imaging of the lung with hyperpolarized 129Xe MRI. Magn Reson Med 2019;81(3):1784–1794. [PubMed: 30346083]
22. Stewart NJ, Leung G, Norquay G, Marshall H, Parra-Robles J, Murphy PS, Schulte RF, Elliot C, Condliffe R, Griffiths PD, Kiely DG, Whyte MK, Wolber J, Wild JM. Experimental validation of the hyperpolarized Xe-129 chemical shift saturation recovery technique in healthy volunteers and subjects with interstitial lung disease. Magn Reson Med 2015;74(1):196–207. [PubMed: 25106025]
23. Hsia CCW, Hyde DM, Weibel ER. Lung Structure and the Intrinsic Challenges of Gas Exchange. Compr Physiol. Volume 62016. p 827–895.
24. Hogg JC, Coxson HO, Brumwell ML, Beyers N, Doerschuk CM, MacNee W, Wiggs BR. Erythrocyte and polymorphonuclear cell transit time and concentration in human pulmonary capillaries. J Appl Physiol 1994;77(4):1795–1800. [PubMed: 7836202]
25. Ruppert K, Mata JF, Brookeman JR, Hagspiel KD, Mugler JP. Exploring lung function with hyperpolarized Xe-129 nuclear magnetic resonance. Magn Reson Med 2004;51(4):676–687. [PubMed: 15065239]
26. Ladefoged J, Andersen AM. Solubility of Xenon-133 at 37$deg$C in Water, Saline, Olive Oil, Liquid Paraffin, Solutions of Albumin, and Blood. Physics in Medicine and Biology 1967;12(3):353–358.
27. He M, Robertson SH, Kaushik SS, Freeman MS, Virgincar RS, Davies J, Stiles J, Foster WM, McAdams HP, Driehuys B. Dose and pulse sequence considerations for hyperpolarized 129Xe ventilation MRI. Magn Reson Imaging 2015;33(7):877–885. [PubMed: 25936684]
28. Pipe JG, Menon P. Sampling density compensation in MRI: Rationale and an iterative numerical solution. Magn Reson Med 1999;41(1):179–186. [PubMed: 10025627]
29. Zwart NR, Johnson KO, Pipe JG. Efficient sample density estimation by combining gridding and an optimized kernel. Magn Reson Med 2012;67(3):701–710. [PubMed: 21688320]
30. Robertson SH, Virgincar RS, He M, Freeman MS, Kaushik SS, Driehuys B. Optimizing 3D noncartesian gridding reconstruction for hyperpolarized 129Xe MRI—focus on preclinical applications. Concept Magn Reson A 2015;44(4):190–202.
31. Stecker IR, Freeman MS, Sitaraman S, Hall CS, Niedbalski PJ, Hendricks AJ, Martin EP, Weaver TE, Cleveland ZI. Preclinical MRI to quantify pulmonary disease severity and trajectories in poorly characterized mouse models: A pedagogical example using data from novel transgenic models of lung fibrosis. Journal of Magnetic Resonance Open 2021;6–7:100013.
32. Hall CS, Quirk JD, Goss CW, Lew D, Kozlowski J, Thomen RP, Woods JC, Tustison NJ, III JPM, Gallagher L, Koch T, Schechtman KB, Ruset IC, Hersman FW, Castro M. Single-Session Bronchial Thermoplasty Guided by 129Xe Magnetic Resonance Imaging. A Pilot Randomized Controlled Clinical Trial. Am J Respir Crit Care Med 2020;202(4):524–534. [PubMed: 32510976]
33. Avants BB, Tustison NJ, Stauffer M, Song G, Wu B, Gee JC. The Insight ToolKit image registration framework. Frontiers in Neuroinformatics 2014;8(44).

34. Taha AA, Hanbury A. Metrics for evaluating 3D medical image segmentation: analysis, selection, and tool. BMC Med Imaging 2015;15:29–29. [PubMed: 26263899]

35. Virtue P, Lustig M. The Empirical Effect of Gaussian Noise in Undersampled MRI Reconstruction. Tomography 2017;3(4):211–221. [PubMed: 29682610]

36. Ruppert K, Brookeman JR, Hagspiel KD, Mugler JP. Probing lung physiology with xenon polarization transfer contrast (XTC). Magn Reson Med 2000;44(3):349–357. [PubMed: 10975884]

37. Rankine LJ, Wang Z, Kelsey CR, Bier E, Driehuys B, Marks LB, Das SK. Hyperpolarized 129Xe magnetic resonance imaging for functional avoidance treatment planning in thoracic radiation therapy: a comparison of ventilation- and gas-exchange-guided treatment plans. International Journal of Radiation Oncology*Biology*Physics 2021.

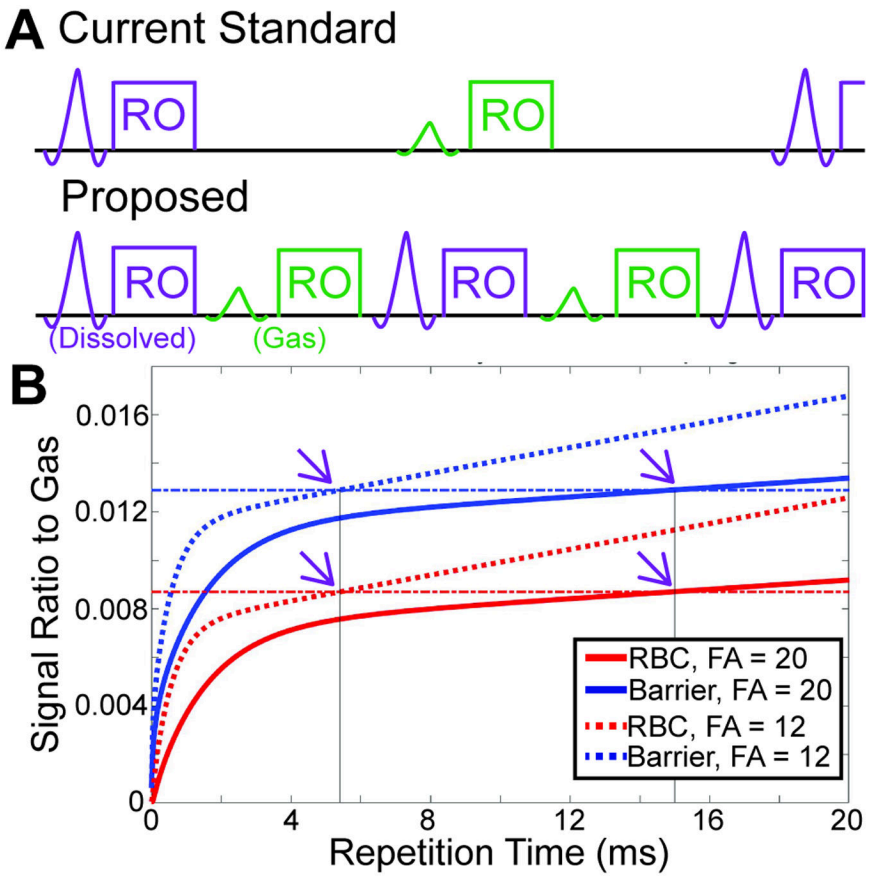


**Figure 1.**

**A** Conceptual sequence diagram showing the "standard" method of gas exchange 1-point Dixon imaging, and the proposed "fast" method. The standard method has a large amount of "dead time" within the sequence, which is reduced in the fast method. Note that only excitation (windowed sinc pulses) and signal readout (RO) are shown in the sequence diagram. **B** Simulations using the model of xenon exchange, show the expected RBC/Gas and Barrier/Gas as a function of repetition time for FA = 20° (solid lines) and FA = 12° (dotted lines). Horizontal dot-dash lines show the magnitude of the simulated RBC/Gas and Barrier/Gas for the standard (FA = 20°, TR = 15 ms) imaging parameters. Solid vertical lines and arrows highlight that RBC/Gas and Barrier/Gas have the same magnitude for the fast (FA = 12°, TR = 5.4 ms) and standard acquisitions.

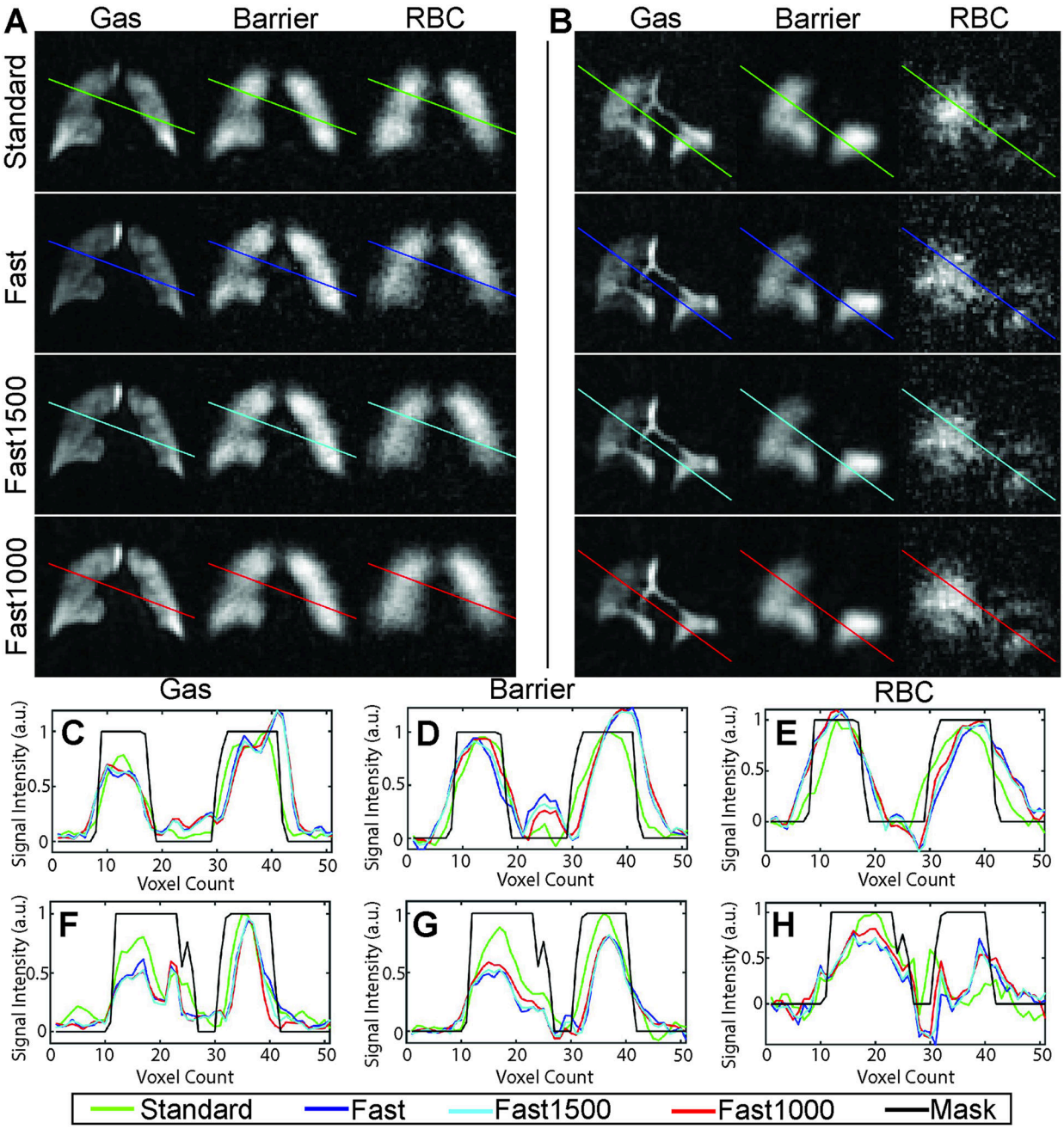


**Figure 2.**

**(A, B)** Representative Ventilation, barrier, and RBC image slices from healthy (**A**) and radiation therapy (**B**) subjects for standard 1-point Dixon imaging parameters and 3 reconstructions of a fast acquisition using different numbers of projections. **C,D,E**: Line profiles are shown for gas, barrier, and RBC images for subject **A**. **F,G,H**: Line profiles are shown for gas, barrier, and RBC images for subject **B**. Images are qualitatively similar, and line profiles show minimal difference between the resolutions of the different images.

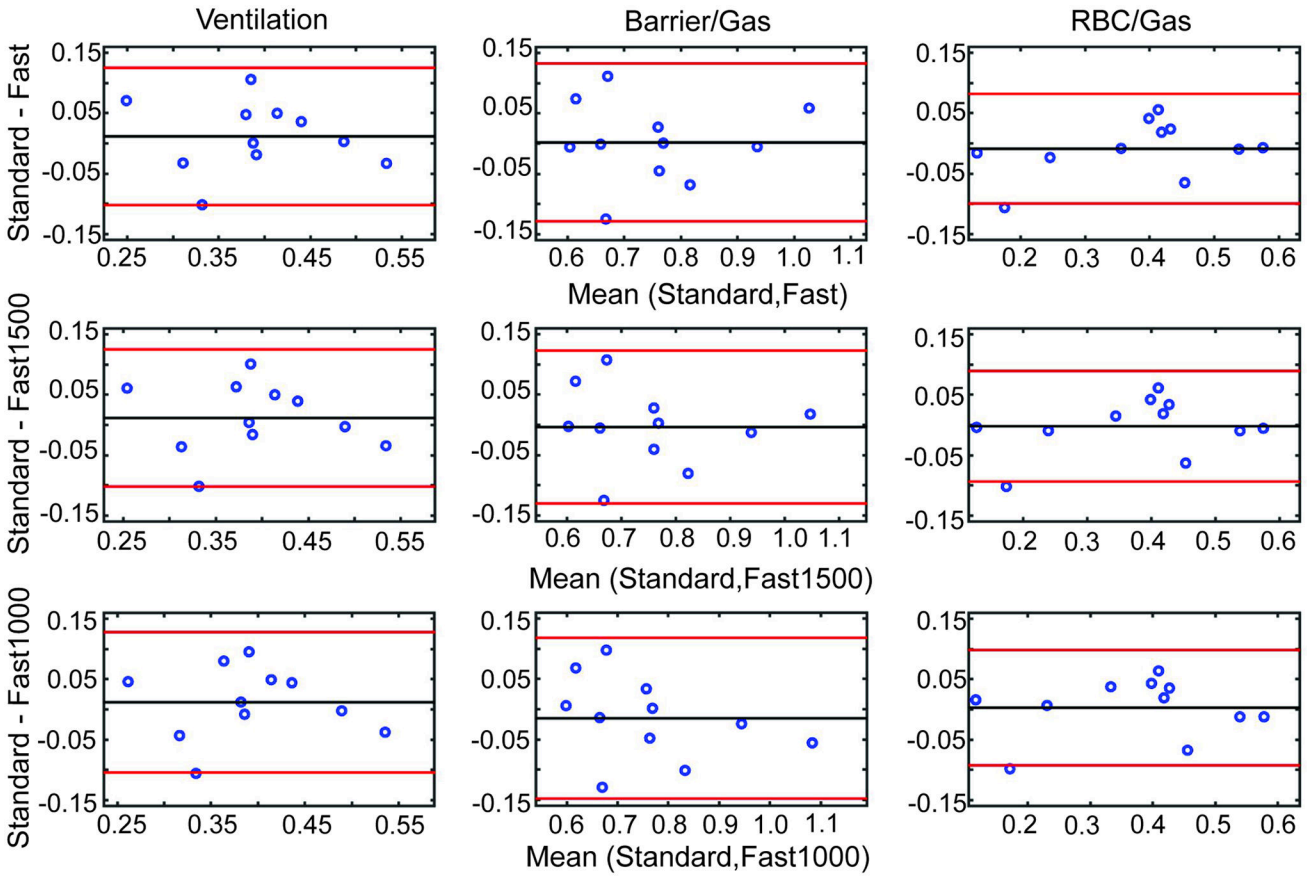


**Figure 3.**

Bland Altman analysis comparing the measurements of mean ventilation (column 1), Barrier/Gas (column 2), and RBC/Gas (column 3). Measurements from Fast (top row), Fast1500 (middle row), and Fast1000 reconstructions are compared to the Standard reconstruction. In every case, the mean difference between measurements is near to 0, which shows that the different imaging parameters and sampling percentages yield similar mean values.

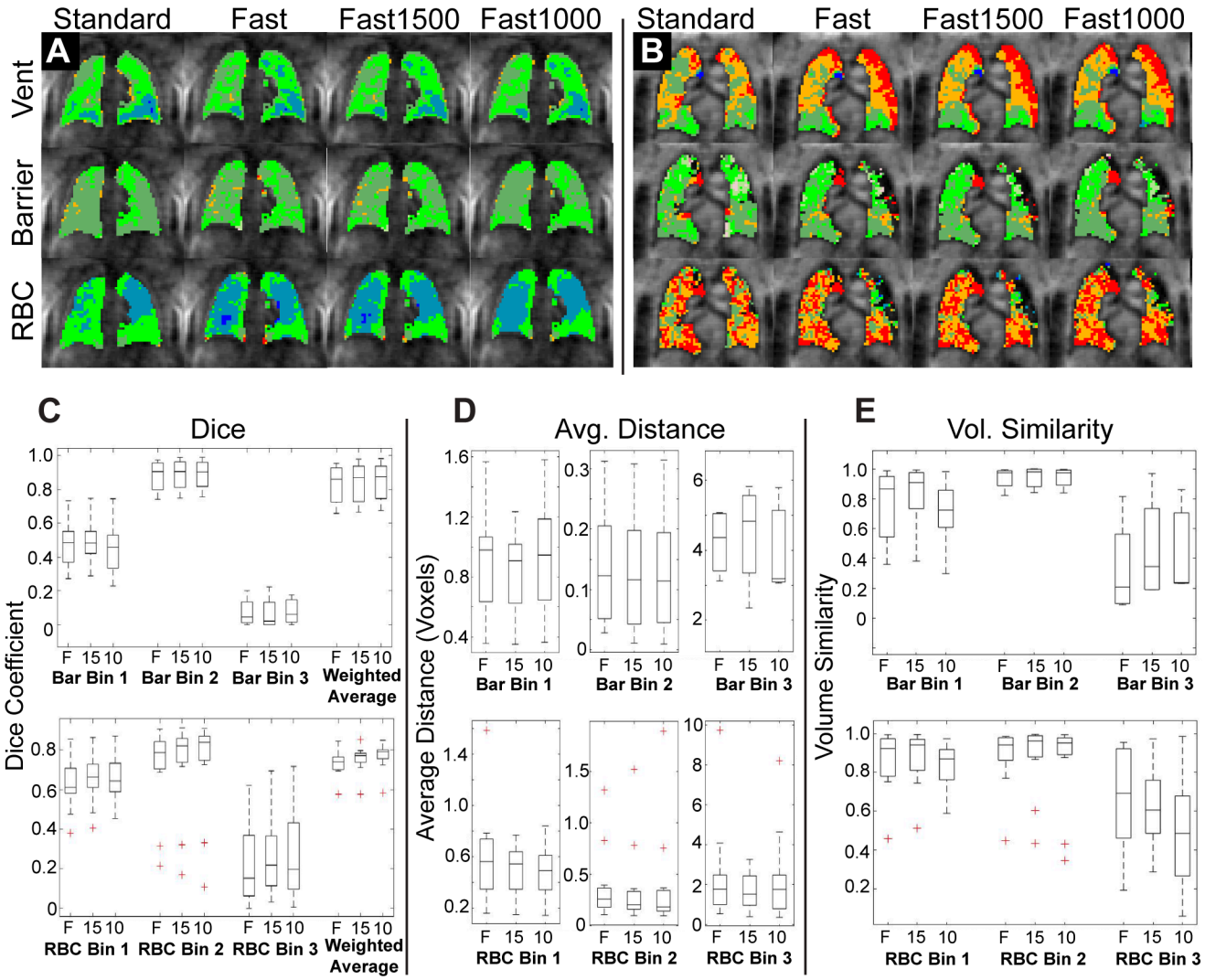


**Figure 4.**

Comparison of binned, registered images. **A, B:** Two representative subjects showing binned Ventilation, Barrier, and RBC images for each of the four image sets. While there are some differences, binning maps are qualitatively similar between standard and fast acquisitions. **C:** Dice coefficients, **D:** Average Distance Metric, and **E:** Volume Similarity Metric comparing the binned fast acquisition to the binned standard acquisition. The three different reconstructions of the fast acquisition are compared to the standard acquisition for barrier (top row) and RBC (bottom row) images. Note that for the average distance metric, distances are measured in voxels rather than mm. F – Fast Acquisition, 15 – Fast Acquisition reconstructed using 1500 radial projections, 10 – Fast Acquisition reconstructed using 1000 radial projections.

**Table 1.**

SNR, whole-lung mean, and whole-lung standard deviation for ventilation, RBC, and Barrier images of healthy subjects. Values are expressed as the cohort mean ± standard deviation. Given similar xenon dose equivalents were given for standard and fast acquisitions (152 and 159 mL), the differences in SNR due to xenon polarization are expected to be minimal. Abbreviations: Vent – Ventilation Image, SNR – Signal to Noise Ratio, RBC – Red Blood Cell

| Scan | Vent SNR | Total Dissolved SNR | Barrier SNR | RBC SNR | Vent Mean | Barrier Mean | RBC Mean | Vent Standard Deviation | Barrier Standard Deviation | RBC Standard Deviation |
|---|---|---|---|---|---|---|---|---|---|---|
| **Standard** | 15±4 | 23±8 | 15±5 | 8±3 | 0.43±0.07 | 0.73±0.10 | 0.45±0.07 | 0.20±0.02 | 0.22±0.11 | 0.25±0.13 |
| **Fast** | 18±5 | 15±6 | 9±4 | 5±2 | 0.41±0.07 | 0.72±0.13 | 0.45±0.08 | 0.22±0.03 | 0.24±0.08 | 0.28±0.09 |
| **Fast1500** | 20±5 | 19±7 | 12±4 | 6±3 | 0.41±0.08 | 0.73±0.13 | 0.44±0.09 | 0.22±0.03 | 0.21±0.08 | 0.24±0.07 |
| **Fast1000** | 21±4 | 23±8 | 15±5 | 8±3 | 0.41±0.07 | 0.73±0.14 | 0.44±0.09 | 0.22±0.03 | 0.18±0.04 | 0.20±0.05 |